Chapter 3 Rotor-axial Eulerian Laser Doppler Vibrometry applied to a single-blade axial-flow test rotor

3.1 Introduction

In this chapter, the application of rotor-axial ELDV to the condition monitoring of axial-flow blades is studied using a single-blade test rotor. ELDV as well as TLDV measurements were recorded at a fixed rotor speed for various damage levels, simulated by means of slot cuts into the blade leading edge close to the blade root. Various signal parameters were considered as possible damage indicators and with the aid of the TLDV measurements, it was found that vibratory phase angle change is indicative of blade damage. After this phenomenon is studied with the aid of FEM simulations, Non-Harmonic Fourier Analysis (NHFA) is studied in depth as a signal processing technique applicable to the ELDV measurements.

NHFA is then applied to the experimental ELDV measurements and is compared with NHFA results from FEM ELDV simulations. It is shown both experimentally and numerically that NHFA applied to rotor-axial ELDV measurements is capable of providing indicators of blade health deterioration.

3.2 Experimental setup

The test rotor depicted in Figure 21 was used to investigate the condition monitoring capabilities of the ELDV measurement technique described in Section 2.4.2. The rotor was driven with a speed-controlled motor and consisted of a solid shaft (supported by two bearings) with a hub and a single flat, straight blade. A Heidenhain ERN 120 shaft encoder provided accurate rotor angular position feedback during testing and the blade was dynamically perturbed during rotation by means of a compressed air-jet. A piezoelectric dynamic pressure sensor installed close to the nozzle, measured the back-pressure at the nozzle arising from the airflow blockage caused by the blade during rotation. Stationary modal testing was performed on the rotor prior to testing for the purpose of FEM updating.

During testing the blade vibrations were measured with a Polytec PSV300 SLDV which was axially aligned with the shaft centre as shown in Figure 22. A sensitivity of 125 mm/s/V was used and the tracking filter option was disabled due to the nature of the measured signals. A 100 kHz low-pass filter was selected on the controller. High-efficiency reflective material was attached to the blade near the blade tip, to

ensure a sufficiently strong LDV signal (Figure 23). Damage was simulated in the test rotor using a slot cut *in situ* into the leading edge of the blade close to the blade root, with slot depth increments of 1 mm, using a 1-mm thick cutting disc on a high-speed rotary tool. This of course is a worst case scenario in terms of blade damage. Since the focus of this thesis is to demonstrate the ELDV measurement technique as a condition monitoring tool, the effects of the location and nature of the damage (i.e. damage simulation that represents cracks more closely) is reserved for further work.

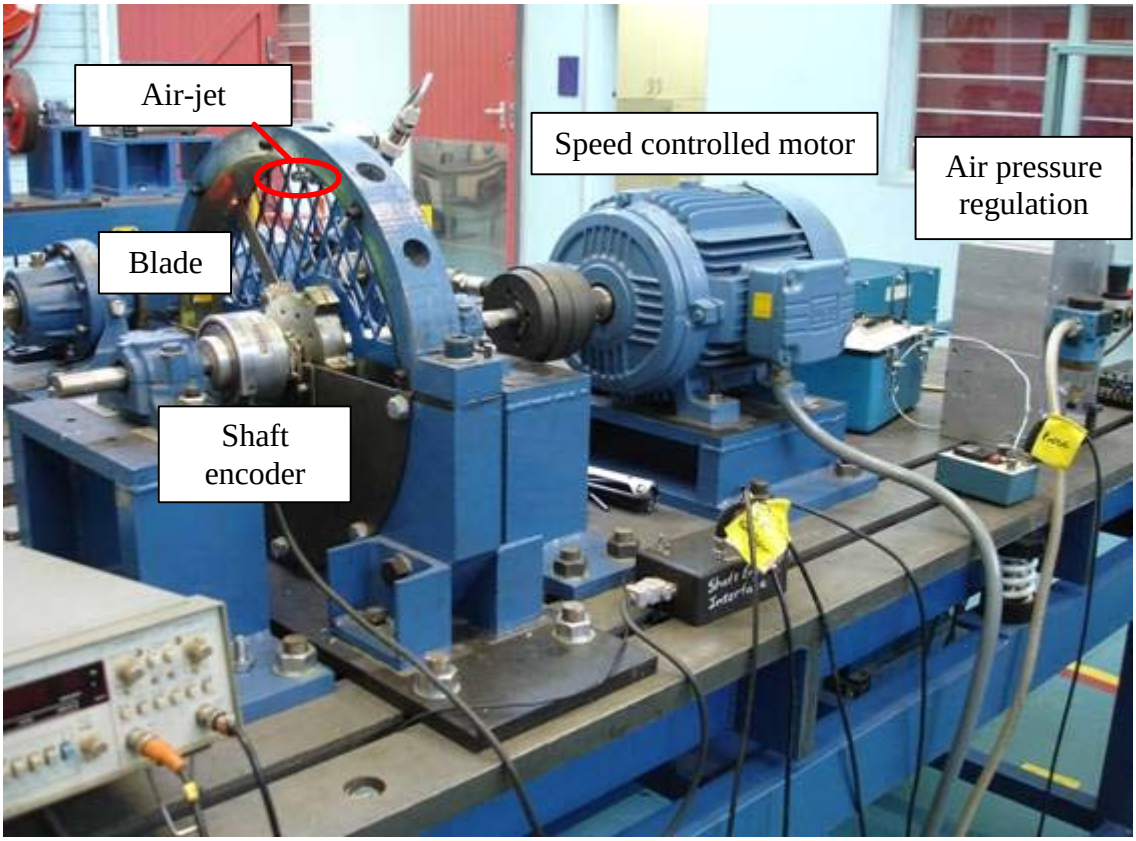

Figure 21: Experimental setup

Figure 22: LDV orientation

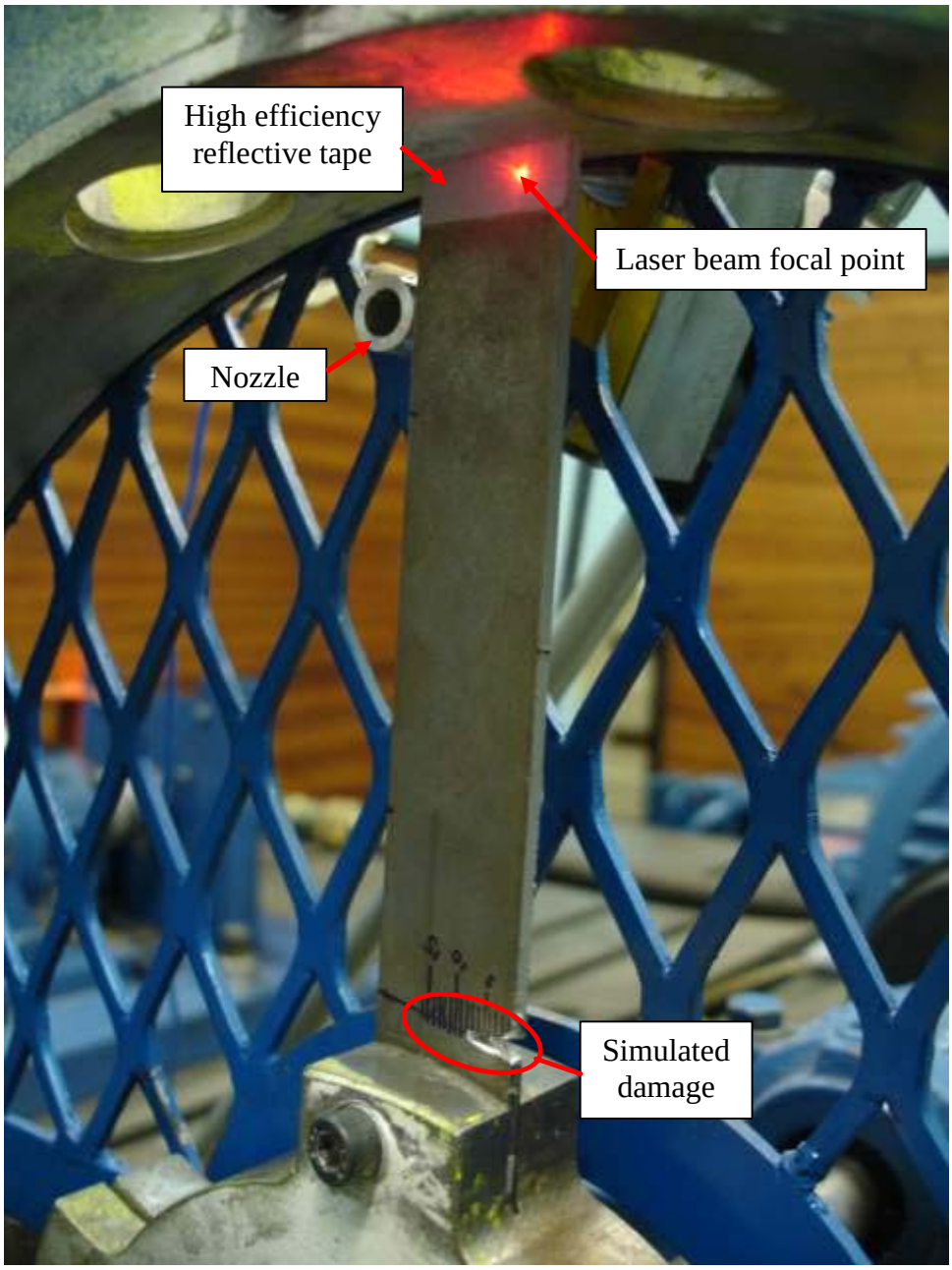

Figure 23: Test setup detail and typical ELDV measurement location

Initial testing was conducted on the rotor at 600 RPM during which only ELDV measurements were recorded. Various signal processing techniques were applied to the measurements, although repeatable results could not be found. These techniques included Burg spectrum estimation, ARMA modelling and AR modelling. Also a frequency domain filter technique was evaluated (Antoni and Randall, 2004a; Antoni and Randall, 2004b).

As the short time span of the ELDV measurements creates difficulties in interpreting the measurements (2.24 ms for 600 RPM resulting in a frequency resolution Δf = 446 Hz), it was decided to record TLDV measurements on the blade during subsequent testing. TLDV is a Lagrangian implementation of laser Doppler vibrometry where the two perpendicular scanning mirrors of the SLDV are controlled to follow a specific point on the rotor during rotation. Thus a vibration signal is yielded over a longer period, giving insight into the dynamic behaviour of the blade during rotation. This furthermore allows the calculation of FFTs and PSDs on the TLDV data with satisfactory frequency resolutions.

3.2.1 Measurement and control

The two scanning mirrors of the Polytec PSV300 vibrometer are mounted on independently controlled servo motors, allowing the mirrors to be tilted on axes perpendicular to each other. The scanning mirror tilt angles (and subsequently the laser beam orientation) can be externally controlled by applying voltage signals to the servo motors. This was performed with a National Instruments PCI-6110 card using the 5000 Pulses-Per-Revolution (PPR) shaft encoder pulses to increment the position of two 90^{o} out-phase sine wave lookup tables, thereby allowing the description of a circular scanning curve as can be seen in Figure 24.

Due to the mechanical response characteristics of the servo-mirror assemblies, it was necessary to adjust the phases and amplitudes of the two control signals for various rotation speeds. In order to streamline the experimental testing procedure, the 1 PPR shaft encoder signal was used to determine the shaft rotation speed. A look-up table containing the various phase angles and amplitudes at predefined rotation speeds was then used for the relevant adjustments.

Control of the National Instruments PCI-6110 card was accomplished with LabView 8, allowing the simultaneous control of the servo motors and the recording of data. A summary of the terminal configuration of the National Instruments connector used is given in Table 4. A sampling frequency of 1 MHz was used to enable the sufficient capturing of the shaft encoder 5000 PPR signal waveform, which had a frequency of about 60 kHz at 720 RPM. The layout of the LabView Virtual Instrument (VI) that was designed consisted of three main sections namely servo motor control, data acquisition and data management as depicted in Figure 25.

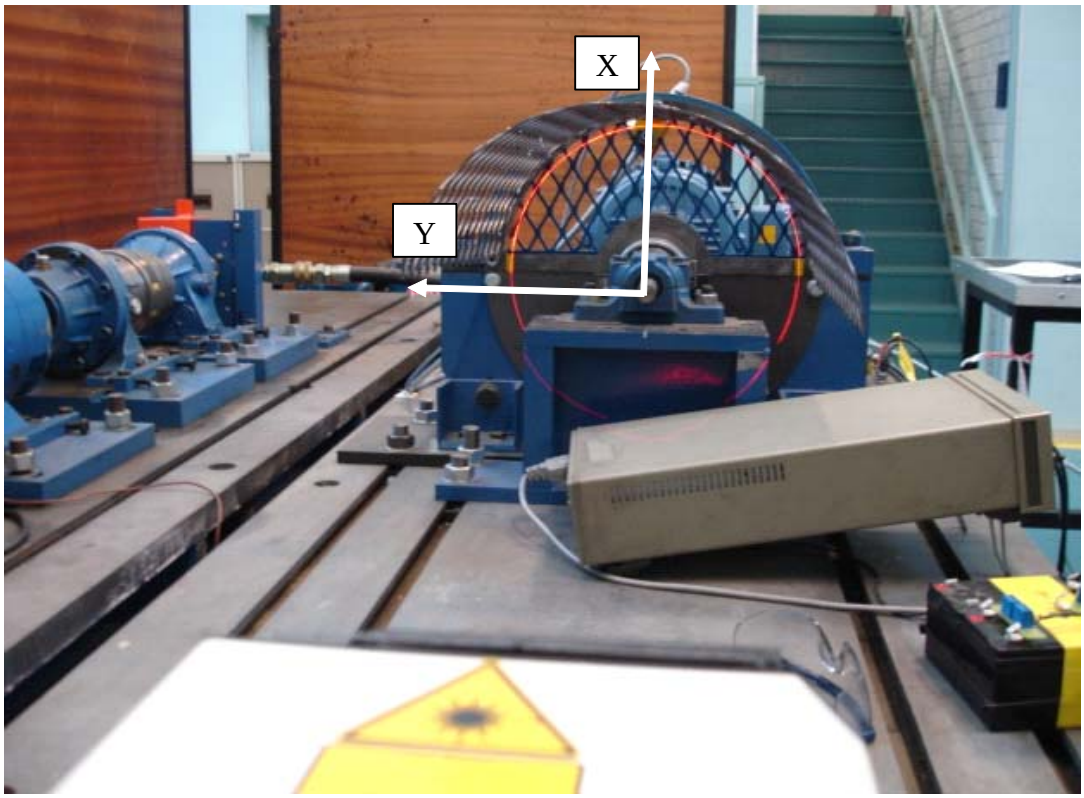

Figure 24: TLDV mirror control

Table 4: National Instruments BNC-2110 terminal configuration

Analogue Inputs
• Dynamics pressure signal
• SLDV signal
• Shaft encoder 5000 PPR signal
• X mirror control signal
Analogue Outputs
• X mirror control signal
• Y mirror control signal
Digital Inputs
• Shaft encoder 1 PPR
o Measurement trigger: Analogue inputs
o Trigger: Mirror control signals
o Rotation speed measurement
• Shaft encoder 5000 PPR
o Clock signal: Mirror control signals

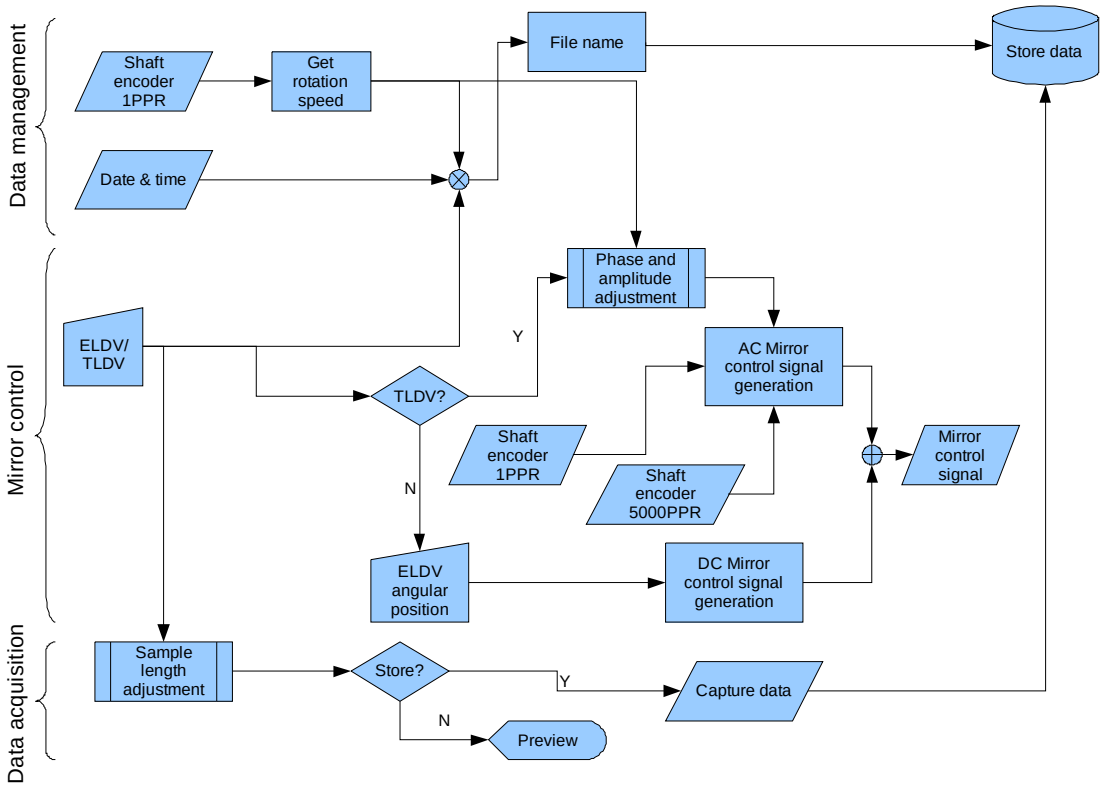

Figure 25: LabView VI flow diagram

An open-loop control methodology was implemented for TLDV control (Figure 25) and as a result the VI was found to have varying lower rotation speed control. Accurate control was possible from 720 RPM and upwards, and for this reason testing was conducted at 720 RPM to obtain the maximum sample lengths. For ELDV measurements DC output signals were supplied to the mirror servo motors corresponding to the desired measurement location. During ELDV measurements, the laser beam was orientated as such as to allow for the measurements to coincide with the positive slopes of the pressure pulses as shown in Figure 26.

3.2.2 Laser alignment

To minimize any TLDV misalignment effects, care was taken in aligning the SLDV with the rotor (Halkon and Rothberg, 2006:1295). Alignment was performed in terms of SLDV pitch, roll and yaw using two approaches. Firstly angular alignment between the SLDV XY-plane and the shaft rotation plane was achieved by controlling the SLDV mirrors to describe a circle with the laser. When misalignment exists, an elliptical scanning curve is observed on the rotor reference plane whereas a circular scanning curve is visible when alignment is sufficient. When the SLDV mirrors are controlled in order to describe a crosshair pattern, it is then possible to align the

SLDV zero position with the shaft centre. The ZX and ZY- planes were also aligned in this way.

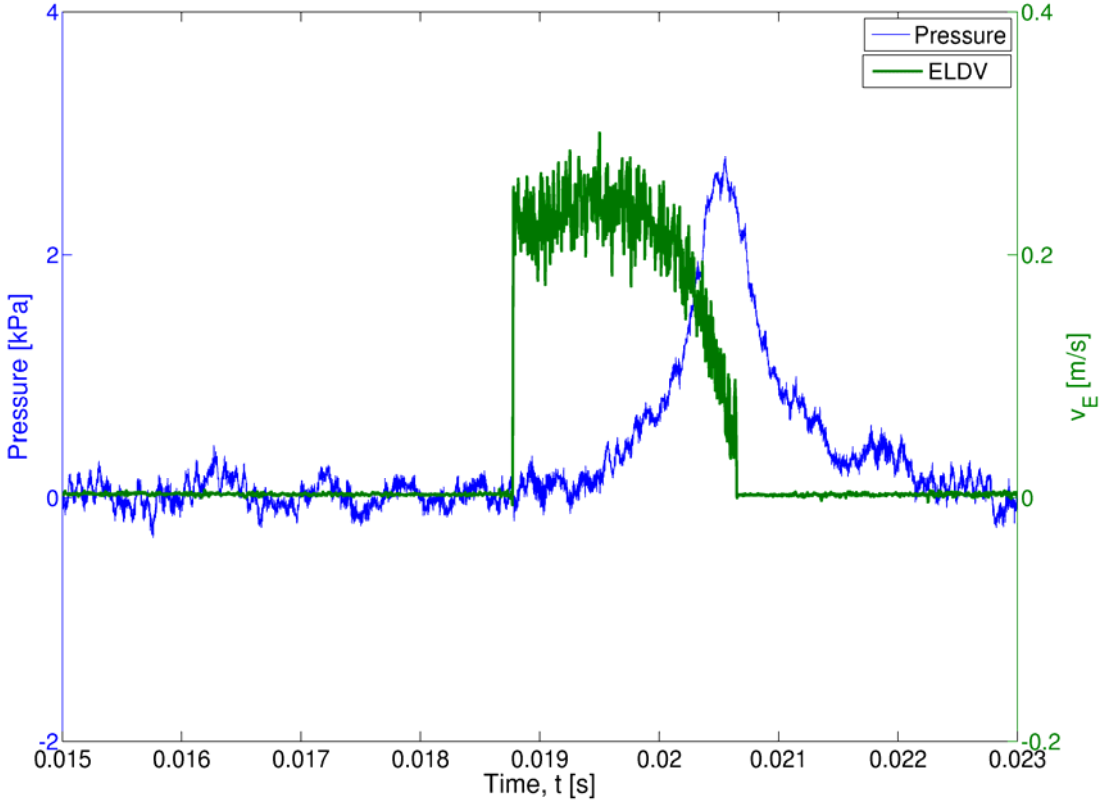

Figure 26: ELDV signature and pressure pulse time histories

Some degree of misalignment is however unavoidable even if great care is taken during the alignment process. According to Halkon and Rothberg (2006) the DC, 1× and 2× components of the scanning frequency (in this case, rotor speed) will be most affected by the misalignment effects. Since these components were well below the first blade bending natural frequency, the TLDV signals were high-pass filtered using a 2nd order Butterworth filter with a cut-off frequency at 50 Hz. Zero-phase digital filtering was employed to eliminate signal phase distortion.

The small misalignment effects will also influence ELDV measurements by introducing a DC component proportional to the rotor speed. Due to the very short nature of the signals considered, it was not possible to high-pass filter the signals without causing signal distortion. Since testing was conducted at a fixed rotor speed, this DC component will be the same in all the measurements. By calculating trends relative to a reference signal, it should be possible to minimize this effect.

3.3 Experimental measurements

The experimental ELDV and TLDV measurements recorded at 720 RPM are depicted in Figure 27(a) and Figure 27(b) respectively for the different damage levels (D_b) considered. Although some amplitude and phase angle changes are visible in the ELDV measurements, it is otherwise difficult to visually interpret the measurements. The TLDV measurements in Figure 27(b) however give further insight into the ELDV measurements. The TLDV measurements are clearly dominated by the first natural frequency of the blade. A systematical change in the vibration phase angle can be observed with increasing damage level except at the 10 mm and 15 mm damage levels. At these two damage levels, phase discontinuities are observed along with sudden amplitude increase (corresponding well with the ELDV measurements). It is shown in Chapter 4 that at both these damage levels, the first blade bending natural frequency has decreased to such extent as to coincide with rotation orders.

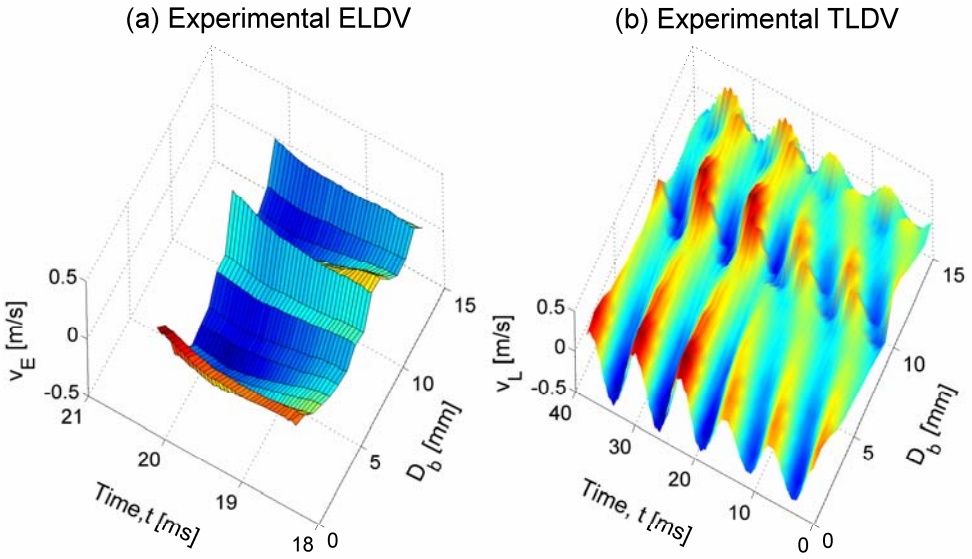

Figure 27: Experimental ELDV and TLDV measurements

3.4 Finite element model

An accurate FEM is required to fully understand the vibration behaviour of the test rotor in terms of its transient responses and natural frequencies. Figure 28 shows the FEM that was constructed using mainly shell and beam elements. A very fine nodal resolution was specified along the corresponding ELDV scanning curve on the FEM for ELDV measurement simulation as depicted in Figure 29(a).

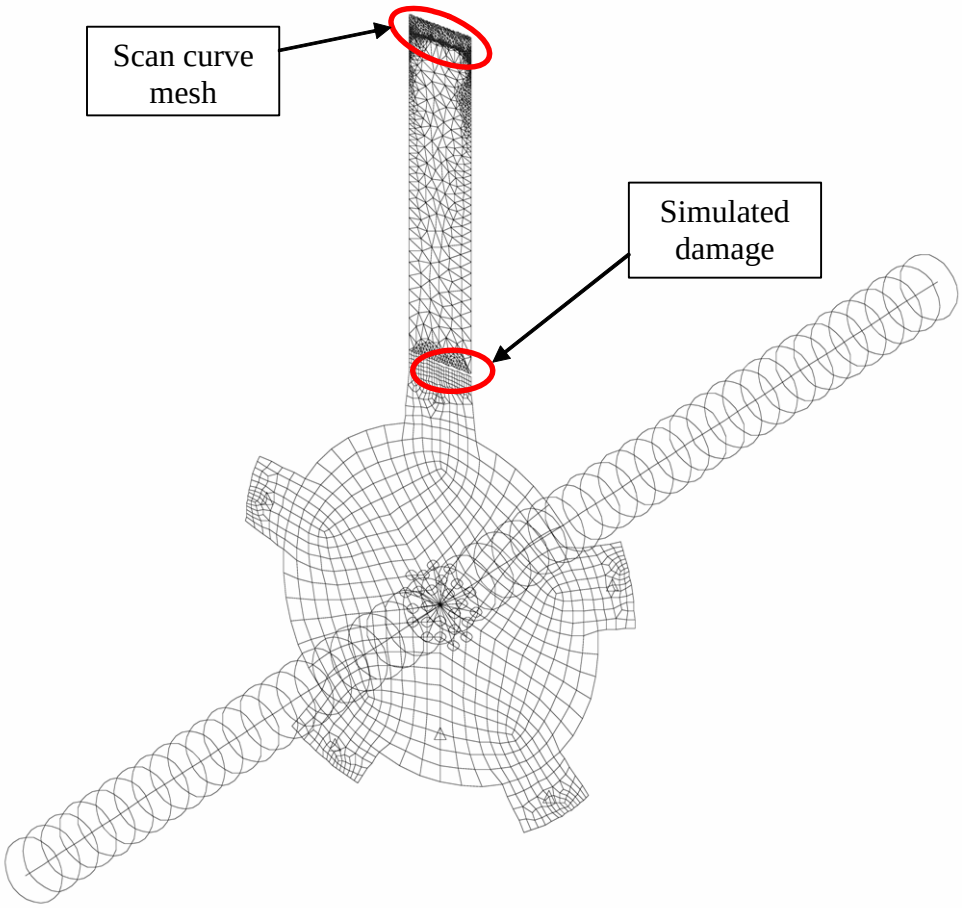

Figure 28: Test rotor FEM

A total of 500 nodes were used along this curve in order to yield an LVRM from which an EVR, containing at least one full period of the blade's first natural frequency, could be directly obtained. To represent the different damage levels induced in the test rotor blade, the element sizes of the FEM at the damage location were chosen so as to allow damage simulation in the FEM by simply deleting the appropriate elements, as shown in Figure 29(b).

Stationary experimental modal testing was conducted on the test rotor using a modal hammer for excitation and a Polytec PDV100 laser vibrometer for measurement of the responses. Following this, FRF-based model updating over a bandwidth of 10 kHz was performed and the results are shown in Figure 30 for the excitation point FRF. The noise that is present in the experimental FRF is attributed to the surface preparation that was used, i.e. developer spray. Opto-reflective material would have

decreased the noise level. The FRF quality was however of sufficiently good quality for the modal updating approach used.

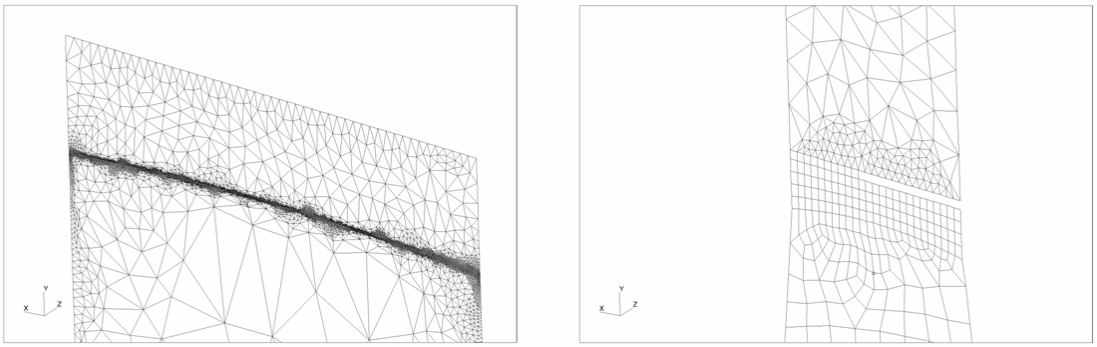

a) Scan curve mesh b) Simulated damage

Figure 29: Mesh resolution at scanning curve

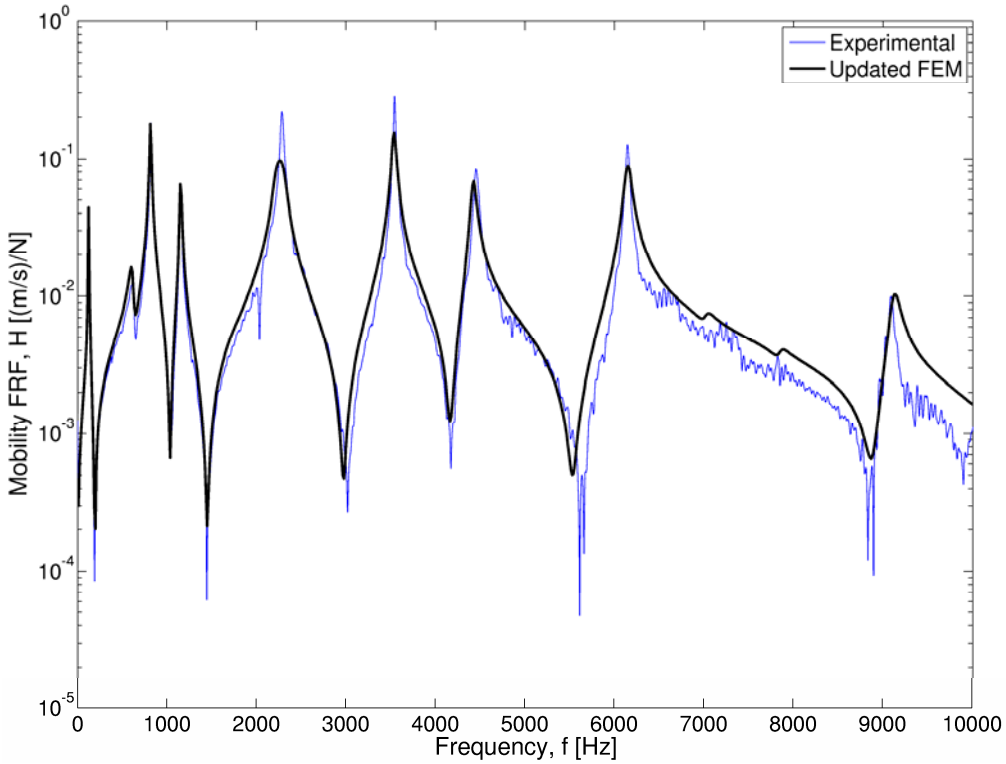

Figure 30: Experimental and FEM FRF comparison

The damage modelling approach in the FEM was also verified by comparing the FEM natural frequencies with the peak frequencies from experimental TLDV PSDs at the various damage levels (Figure 31). This figure shows clear correlation in terms of

frequency shifts, indicating that the FEM was successfully updated and that the FEM damage modelling was representative of experimental damage.

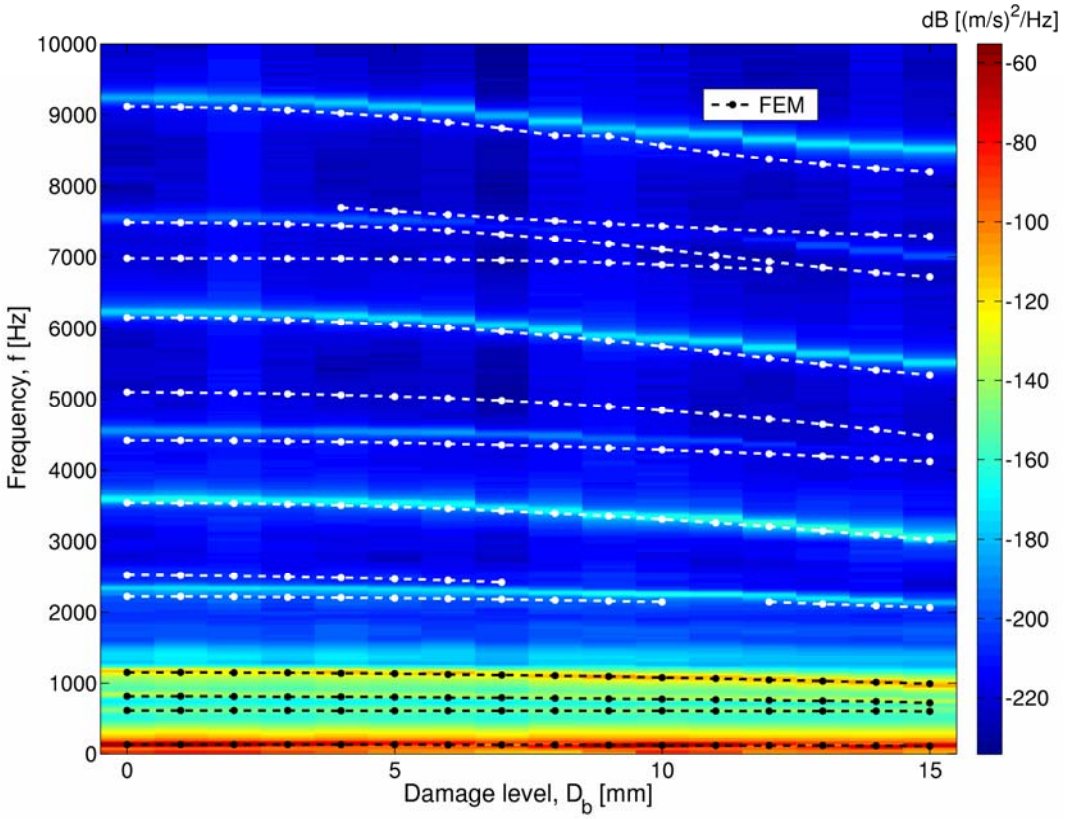

Figure 31: Validation of the FEM damage simulation technique

A linear relationship was found between the air-jet and impact hammer excited responses with the aid of appropriate experimental FRF measurements. Since only linear analysis was used in the FEM calculations, the responses obtained from the FEM could easily be scaled in amplitude to match the experimental measurements. The excitation provided by the air-jet nozzle during rotation was approximated by a single force at a location on the FEM blade, matching the angular position at which the experimentally measured nozzle back-pressure peaked.

Two approaches were evaluated to obtain TLDV and ELDV simulations. The first approach was to perform transient analyses using an average measured nozzle pressure signal as an input force with the FEM initially at rest. The results of the transient analyses on the FEM exhibited the participation of sideways blade vibration modes in the rotor-axial direction. This phenomenon is an artefact of the angular offset between the blade-bending neutral axis and the measurement plane. Since the LDV in use only measures out-of-plane vibrations (within a $\pm 20^o$ angular offset

range), these modes have to be discarded to facilitate comparison with the experimental results.

When calculating the FRFs directly from the FEM in the rotor-axial direction, it is possible to suppress the participation of the sideways vibration modes. Using impulse response function calculations on the FRFs, PSDs can be subsequently calculated and scaled. Figure 32 compares the PSD of FEM-simulated TLDV with that from experimental TLDV measurements for an undamaged blade. Good correlation with regards to peak frequency location is observed.

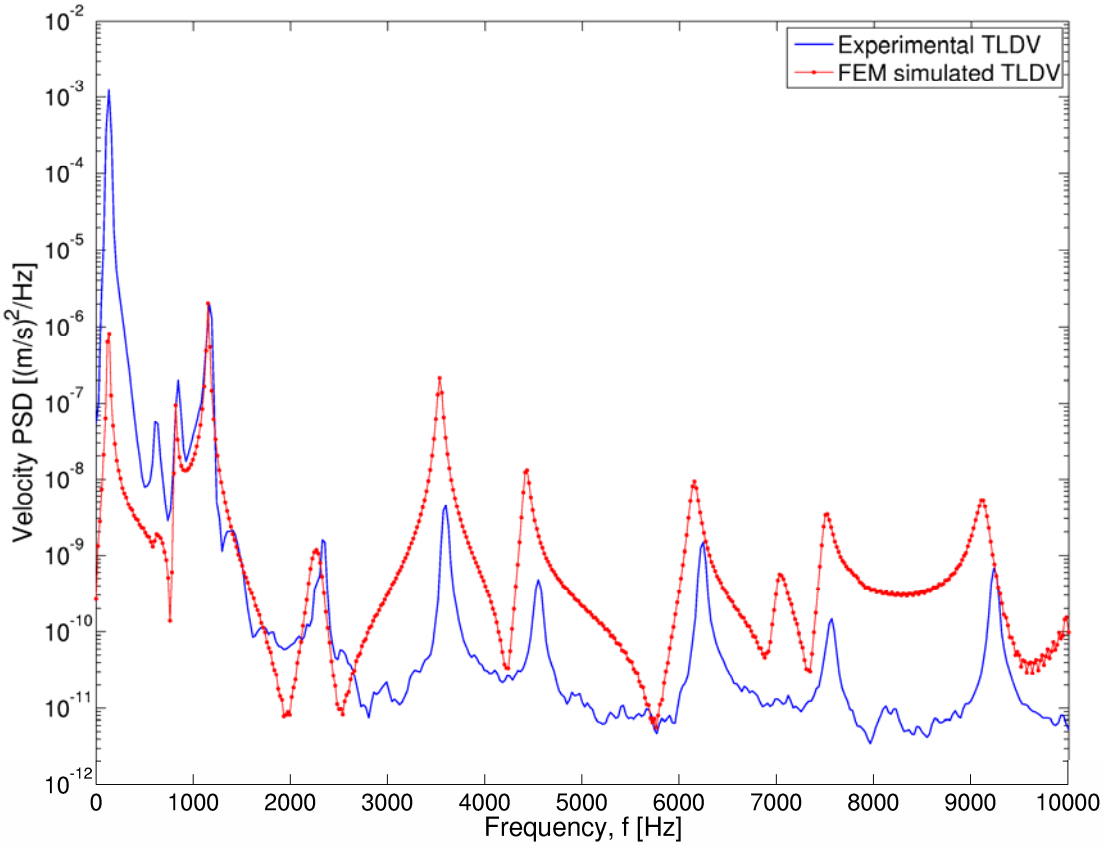

Figure 32: Comparison of experimental and FEM TLDV PSDs

To compare the simulated ELDV time responses with experimental measurements, amplitude-normalized response surfaces are constructed as indicated in Figure 33. Although the correlation is not particularly strong, similar trends are visible. The discrepancies may be attributed to the FEM ELDV simulation approach, which constitutes of impulse responses from calculated FRFs. Thus in comparison to the experimental measurements, the FEM results contain transient vibration behaviour more strongly. Although the damage modelling approach has been validated, small

differences between experimental and FEM damage levels were unavoidable. This will also cause discrepancies between the results.

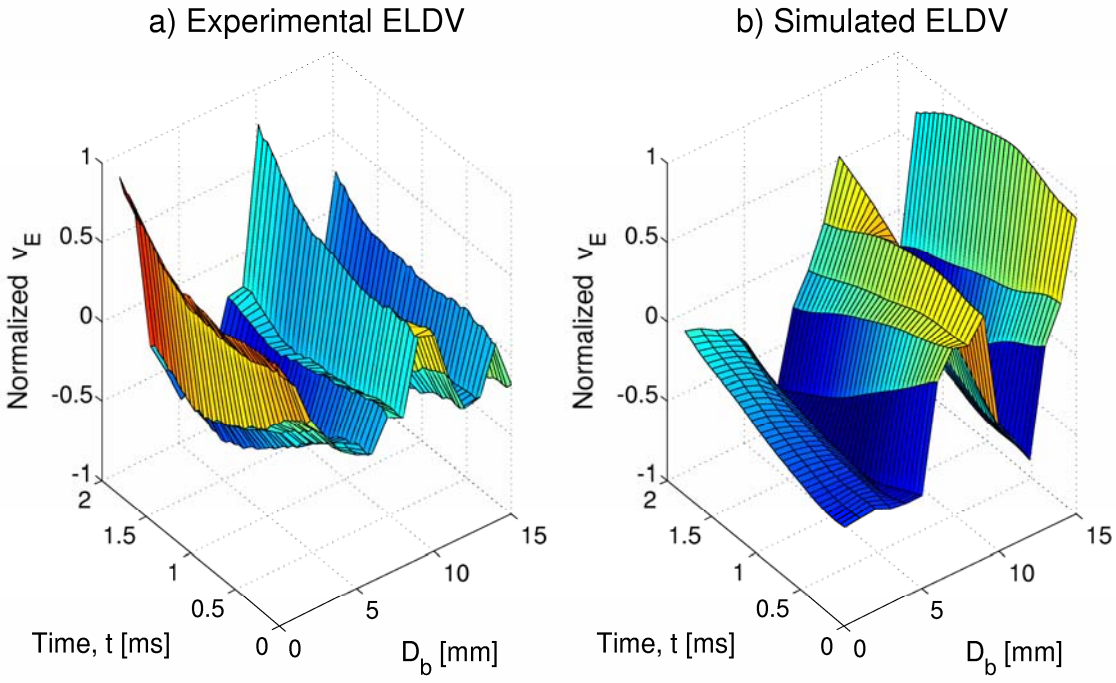

Figure 33: Response surface comparison

3.5 Phase angle as a damage indicator

A systematical change in the vibration phase angle with increasing damage level was observed from the experimental TLDV measurements (Figure 27). Although the applications differ, various literature sources report on using vibratory phase angle as a damage indicator (Jacobs and De Roeck, 2003; King et al., 2006). To investigate this phenomenon for the application this thesis is concerned with, FFTs of simulated TLDV responses were calculated for various damage levels.

Figure 34 shows the FFTs for the first bending natural frequency of the blade. Frequency shifts with increasing damage level are observed albeit small, while the phase angles at the various peak frequencies remain relatively constant. A clear trend is present when the various phase angles are considered at a fixed reference frequency (in this case the peak frequency for the undamaged case). Figure 35 compares the peak frequency and phase angle trend shifts with the latter expressed as a percentage of the total phase angle change around a natural frequency, i.e. 180^o.

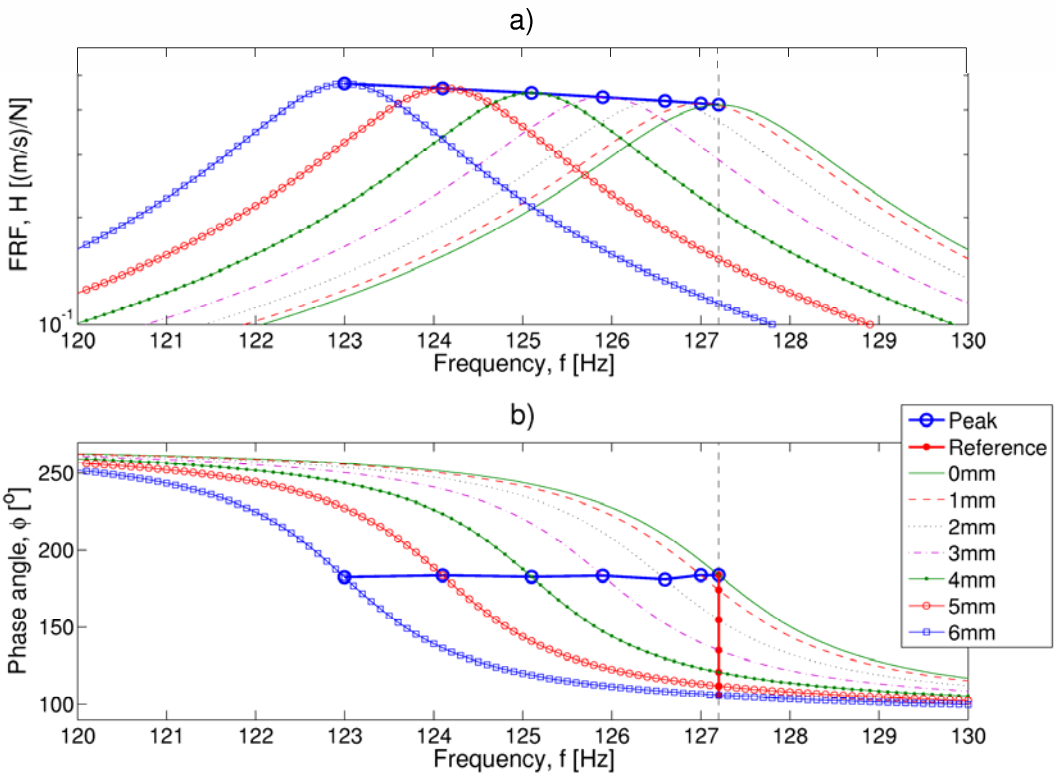

Figure 34: Influence of damage level on peak frequency and phase angle

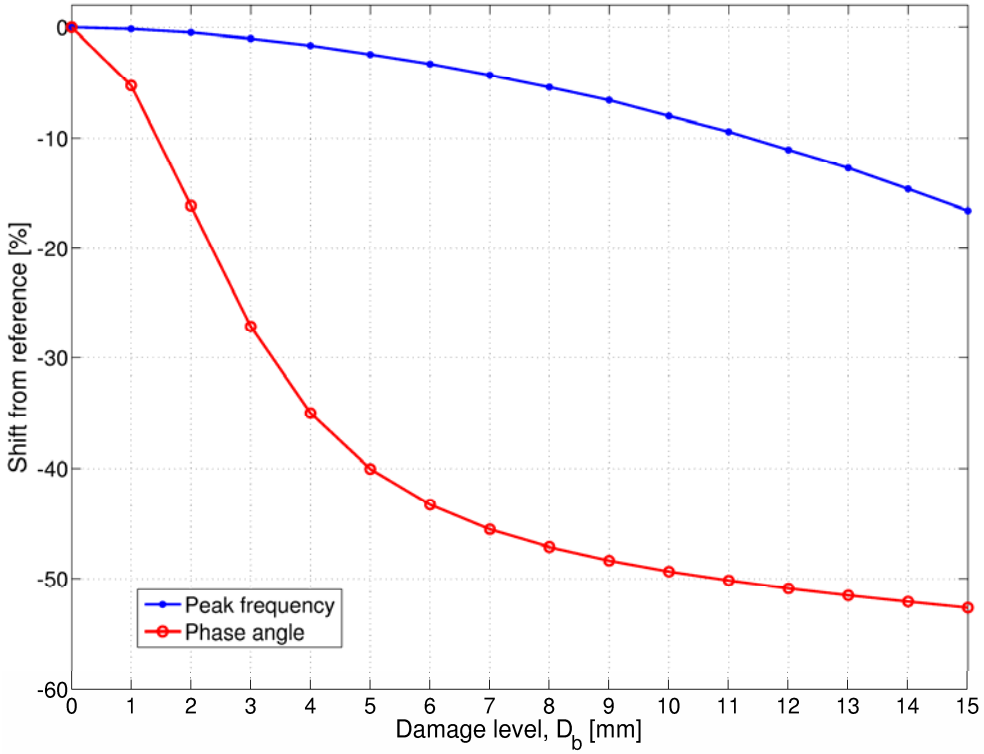

Figure 35: Comparison between peak frequency shift and phase angle shift

From these results and the experimental TLDV measurements, it is clear that phase angle trends of blade vibration signals can indeed be used for condition monitoring purposes. It is thus desirable to extract phase-related information from the ELDV measurements. However the problem remains as how to obtain this information from such short signals. One signal processing technique suitable for this task is NHFA which is discussed in detail in the following section.

3.6 Non-Harmonic Fourier Analysis

Similarly to HFA, NHFA approximates the signal with sine and cosine components although NHFA requires additional normalization components (Hirata, 2005). It is necessary to perform signal component separation to obtain accurate results, although signal components need to be separated by up to 1.6 of the fundamental frequency of the signal to be able to do this (Muraoka and Nishioka, 2004). This requirement renders the signal separation approach proposed by Hirata (2005) impractical for the experimental ELDV measurements based on the stationary modal analysis results. However as shown in this section, this lack of signal separation can be exploited for the purpose of condition monitoring, as it is possible to use the NHFA phase angle at a reference frequency as an indicator of both signal phase angle and frequency shifts.

In HFA, Fourier components are expressed at integer multiples m of the signal fundamental frequency ϖ_0 (in radians per second) in terms of cosine and sine coefficients as shown for an arbitrary time signal y (Rao, 1995:58):

$$y(t) = \frac{a_0}{2} + \sum_{m=1}^{\infty} \left(a_m \cos m\varpi_0 t + d_m \sin m\varpi_0 t \right)$$

Equation 22

with the respective cosine and sine coefficients

$$a_m = \frac{2}{\tau} \int_0^{\tau} y(t) \cos m\varpi_0 t \, dt = \frac{2}{\tau} \int_{-\tau/2}^{\tau/2} y(t) \cos m\varpi_0 t \, dt$$

$$d_m = \frac{2}{\tau} \int_0^{\tau} y(t) \sin m\varpi_0 t \, dt = \frac{2}{\tau} \int_{-\tau/2}^{\tau/2} y(t) \sin m\varpi_0 t \, dt$$

Equation 23

and $\varpi_0 = 2\pi/\tau$ radians while τ is the total signal time span. The $2/\tau$ constant in Equation 23 serves to normalize the integrals in terms of τ.

Consider a monotone signal with a harmonic frequency $m\varpi_0$ and arbitrary phase angle ϕ:

$$y(t) = \cos(m\varpi_0 t + \phi)$$

Equation 24

Evaluating Equation 23 at $m\varpi_0$, the coefficients reduce to:

$$a_m = \cos\phi$$
$$d_m = -\sin\phi$$

Equation 25

When NHFA is considered, the signal under investigation is also described in terms of cosine and sine coefficients. At an arbitrary frequency ϖ, the signal under examination is then approximated in terms of n as shown by Hirata (2005):

$$G(n,\varpi) = a(\omega)\times C(n,\varpi) + d(\varpi)\times S(n,\varpi)$$

Equation 26

with the respective cosine and sine coefficients

$$a(\varpi) = \sum_{n=0}^{N} y(n)\times C(n,\varpi) \Big/ \sum_{n=0}^{N} C(n,\varpi)^2$$
$$d(\varpi) = \sum_{n=0}^{N} y(n)\times S(n,\varpi) \Big/ \sum_{n=0}^{N} S(n,\varpi)^2$$

Equation 27

and

$$C(n,\varpi) = \cos[(n - N/2)\varpi / f_s]$$
$$S(n,\varpi) = \sin[(n - N/2)\varpi / f_s]$$

Equation 28

Since $n = 0,1,...,N$ corresponds to the time signal data sequence, Hirata (2005) effectively considers the signal over a time span of $t = -\tau/2,...,\tau/2$.

To gain insight into the NHFA technique, it is useful to consider Equation 27 analytically (Oberholster and Heyns, 2008):

$$a(\varpi) = \int_{-\tau/2}^{\tau/2} y(t)\cos(\varpi t)dt \Big/ \int_{-\tau/2}^{\tau/2} \cos^2(\varpi t)\,dt$$
$$d(\varpi) = \int_{-\tau/2}^{\tau/2} y(t)\sin(\varpi t)dt \Big/ \int_{-\tau/2}^{\tau/2} \sin^2(\varpi t)\,dt$$

Equation 29

When the nominators of Equation 29 are evaluated for a monotone signal $y(t) = \cos(\varpi t + \phi)$:

$$a(\varpi)_{NOM} = \int_{-\tau/2}^{\tau/2} y(t)\cos(\varpi t)dt = \cos\phi\left[\frac{\varpi\tau + \sin\varpi\tau}{2\varpi}\right]$$
$$d(\varpi)_{NOM} = \int_{-\tau/2}^{\tau/2} y(t)\sin(\varpi t)dt = -\sin\phi\left[\frac{\varpi\tau - \sin\varpi\tau}{2\varpi}\right]$$

Equation 30

The evaluation of the denominators yield:

$$a(\varpi)_{DEN} = \int_{-\tau/2}^{\tau/2} \cos^2(\varpi t)\,dt = \frac{\varpi\tau + \sin\varpi\tau}{2\varpi}$$
$$d(\varpi)_{DEN} = \int_{-\tau/2}^{\tau/2} \sin^2(\varpi t)\,dt = \frac{\varpi\tau - \sin\varpi\tau}{2\varpi}$$

Equation 31

and thus

$$a(\varpi) = a(\varpi)_{NOM} / a(\varpi)_{DEN} = \cos\phi$$
$$d(\varpi) = d(\varpi)_{NOM} / d(\varpi)_{DEN} = -\sin\phi$$

Equation 32

which is identical to the result of HFA in Equation 25.

The component phase angle obtained with NHFA Φ is given by:

$$\Phi(\varpi) = \tan^{-1}\left[\frac{-d(\varpi)}{a(\varpi)}\right]$$

Equation 33

3.6.1 Signal shift detection using NHFA

As discussed in Section 3.5, phase angle can be used as a frequency shift indicator when tracked at a fixed reference frequency. To study this application using NHFA, consider a signal with an arbitrary frequency removed $\Delta\varpi$ from a reference frequency ϖ_{ref} and an arbitrary phase angle ϕ:

$$y(t_0) = \cos\left[\left(\varpi_{ref} + \Delta\varpi\right)t_0 + \phi\right]$$

Equation 34

with $t_0 = 0, ..., \tau$ as with an actual measured signal.

As the time span used in NHFA is defined as $t = -\tau/2, ..., \tau/2$, Φ yields the phase angle of the component under consideration at the mid-span of the time vector, i.e. at $t = 0$. When a signal is expressed in terms of $t_0 = 0, ..., \tau$, Φ thus gives the component phase angle at $t_0 = \tau/2$. In order to obtain Φ at $t_0 = 0$, two phase angle correction steps are necessary when analytical NHFA is employed.

Firstly to transform the signal from t_0 to t, it is necessary to compensate for the resulting phase lag that is introduced. This phase lag is simply given by half the product of the signal frequency and time span:

$$\phi_{lag} = \left(\varpi_{ref} + \Delta\varpi\right)\tau/2$$

so that

$$y_{t_0 \Rightarrow t}(t) = \cos\left[\left(\varpi_{ref} + \Delta\varpi\right)\cdot t + \phi + \phi_{lag}\right] = \cos\left[\left(\varpi_{ref} + \Delta\varpi\right)\cdot t + \phi + \left(\varpi_{ref} + \Delta\omega\right)\tau/2\right]$$

Equation 35

Evaluating Equation 29 for this case:

$$a\left(\varpi_{ref}\right) = \left(\frac{2\varpi_{ref}}{\varpi_{ref}\tau + \sin\varpi_{ref}\tau}\right)\left[\frac{\sin\left(\Delta\varpi\tau/2\right)}{\Delta\varpi} + \frac{\sin\left(2\varpi_{ref} + \Delta\varpi\right)\tau/2}{2\varpi_{ref} + \Delta\varpi}\right]\cos\left[\phi + \left(\varpi_{ref} + \Delta\varpi\right)\tau/2\right]$$

$$d\left(\varpi_{ref}\right) = -\left(\frac{2\varpi_{ref}}{\varpi_{ref}\tau - \sin\varpi_{ref}\tau}\right)\left[\frac{\sin\left(\Delta\varpi\tau/2\right)}{\Delta\varpi} - \frac{\sin\left(2\varpi_{ref} + \Delta\varpi\right)\tau/2}{2\varpi_{ref} + \Delta\varpi}\right]\sin\left[\phi + \left(\varpi_{ref} + \Delta\varpi\right)\tau/2\right]$$

Equation 36

and

$$\Phi_{\varpi_{ref}} = \tan^{-1}\frac{-d\left(\varpi_{ref}\right)}{a\left(\varpi_{ref}\right)}$$

Equation 37

Secondly, $\Phi_{\varpi_{ref}}$ also needs to be adjusted:

$$\Phi_{\varpi_{ref},t_0} = \Phi_{\varpi_{ref}} - \varpi_{ref}\,\tau/2$$

Equation 38

Only the second correction step is required when NHFA is employed numerically.

From Equation 36 and Equation 37, it is observed that $\Phi_{\varpi_{ref}}$ (and thus Φ_{ϖ_{ref},t_0} as well) is influenced by both frequency and phase shifts in the signal. It is thus indeed possible to detect vibration changes in a signal by monitoring $\Phi_{\varpi_{ref}}$.

3.6.2 Sensitivity analysis

To determine the sensitivity of Φ_{ϖ_{ref},t_0} to phase and frequency shifts in a signal, a sensitivity analysis was performed.

Firstly, phase angle shift is considered in a monotone signal while the signal's frequency is kept constant. Figure 36(a) shows the results for both analytic and numeric NHFA for a phase angle shift from -180^o to 180^o in a 10.1 Hz sinusoidal signal with τ = 1 s. Figure 36(b) provides the phase angle error of the analytic and numeric approach relative to the actual signal phase angle, showing both formulations to be accurate.

Figure 37 to Figure 39 present results for various cases. In these three figures, the (a) subplots depict the numerical formulation results. The (b) subplots show the difference of the analytical formulation phase angles from those of the numerical formulation, thereby evaluating the validity of the analytical formulation at each of these cases.

When only frequency shift is considered (i.e. the signal phase angle is kept constant), Figure 37 is obtained for two ϖ_{ref} s at 10 Hz and 10.25 Hz respectively, with the actual signal frequency ranging from 6.5 Hz to 13.5 Hz. The horizontal axes express $\Delta\varpi$ in terms of ϖ_0, which for the analyzed signal is 1 Hz. Figure 37(a) shows that the relationship between Φ_{ϖ_{ref},t_0} and $\Delta\varpi$ is approximately linear for sections in bands of integer values for $\Delta\varpi/\varpi_0$. In fact for $-\varpi_0 < \Delta\varpi < \varpi_0$, Φ is approximately $\pi \cdot \Delta\varpi/\varpi_0$. When $\Delta\varpi = m\varpi_0$, 180^o phase angle jumps are visible and upon further investigation it is observed that both the sine and cosine coefficients either approach

or cross zero in this vicinity. Also, it is shown that when ϖ_{ref} is not an integer multiple of ϖ_0, the phase angle jumps are not as abrupt.

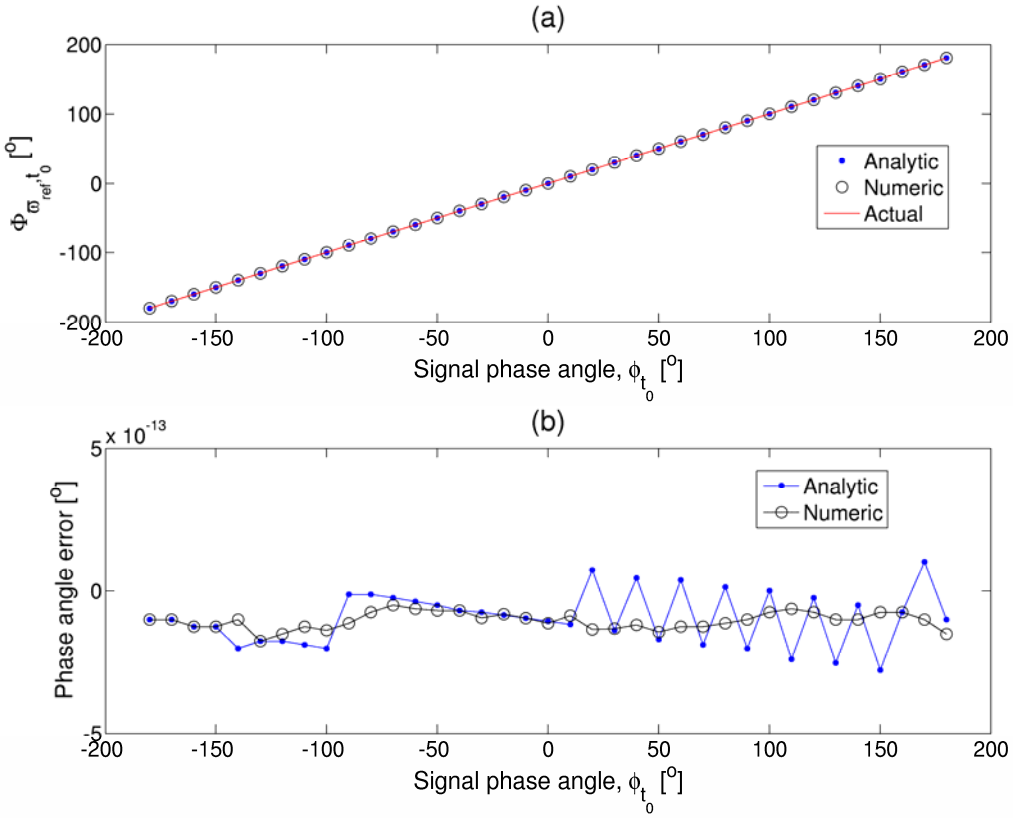

Figure 36: Phase angle shift

In Figure 37(b), the phase angle differences between the analytical and numerical results are shown to increase with frequency offset. Furthermore it is noted that at harmonics of the fundamental frequency, these differences are largely influenced by the reference frequency.

For more extreme values of $\Delta\varpi$, it is clear that Φ loses its linear relationship to $\Delta\varpi/\varpi_0$ as shown in Figure 38(a). In this figure the legend indicates the various signal frequencies that need to be added to the normalized frequency offset factor in order to give the actual signal frequency, e.g. the signal frequency for the 50 Hz curve ranges from 50 Hz to 51 Hz. Noted from Figure 38(b) is that the analytical form of NHFA becomes less and less representative of the numerical form as $\Delta\varpi$ increases.

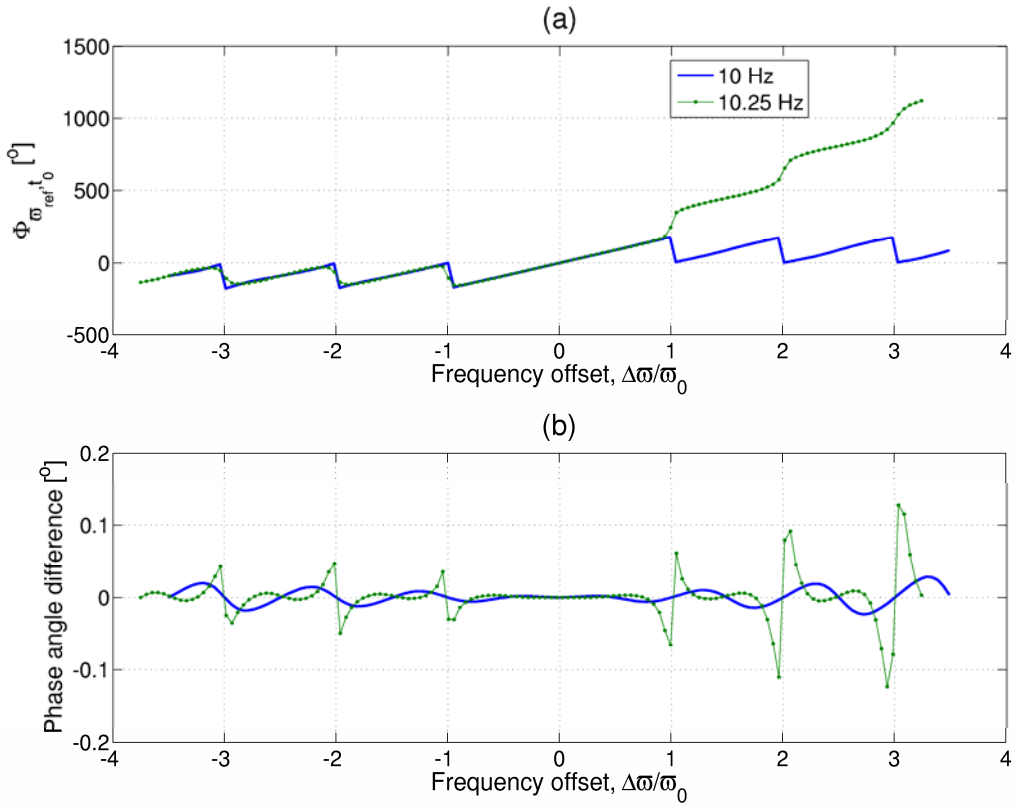

Figure 37: Effect of frequency shift

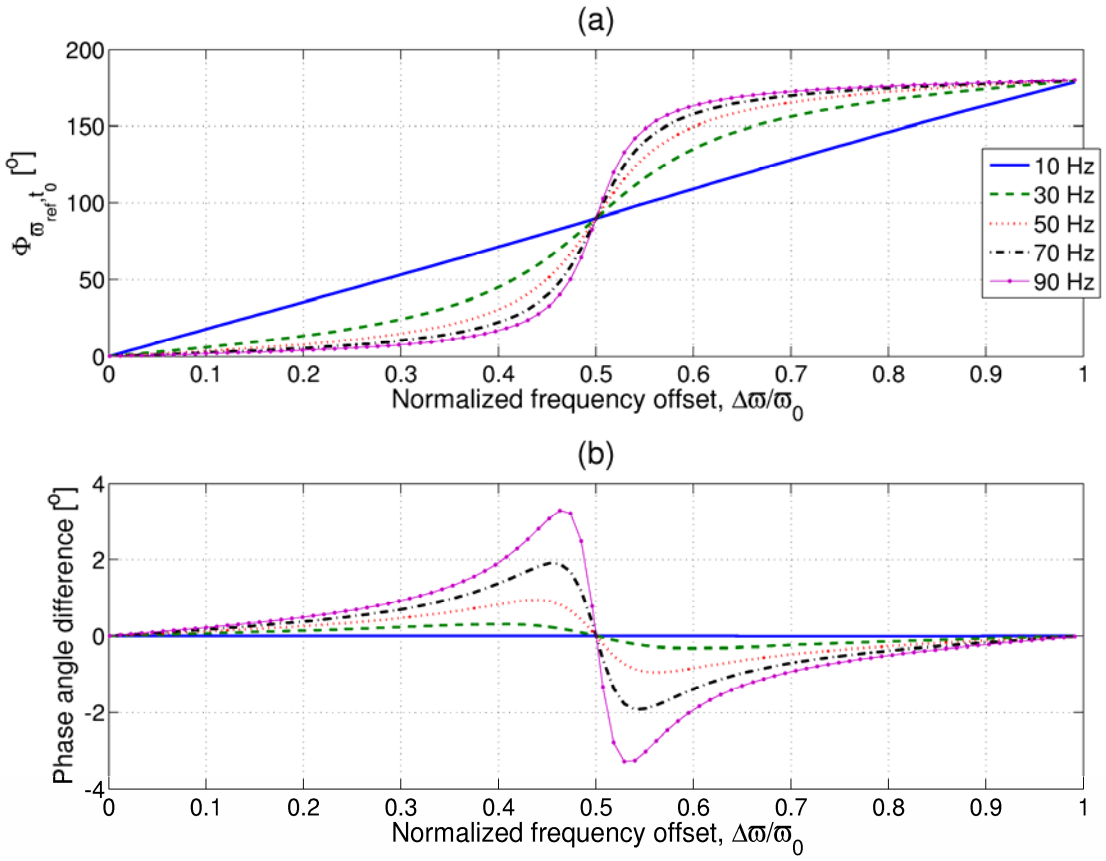

Figure 38: Effect of frequency shift at higher frequency offsets

Figure 39(a) depicts the effect of $\Delta\varpi$ on the accuracy of phase angle detection. As can be noted from this figure, a sign error may occur (although not always) in Φ when $\Delta\varpi = m\varpi_0$. Figure 39(b) shows a more acceptable deviation of the analytical results from the numerical results.

From Figure 37(b), Figure 38(b) and Figure 39(b) the analytical formulation is shown to be representative of the numerical formulation only for low frequency offsets, excluding situations where $\Delta\varpi$ is close to an integer multiple of ϖ_0. The existence of these discrepancies can be ascribed to the different integration techniques used in the numerical and analytical formulations.

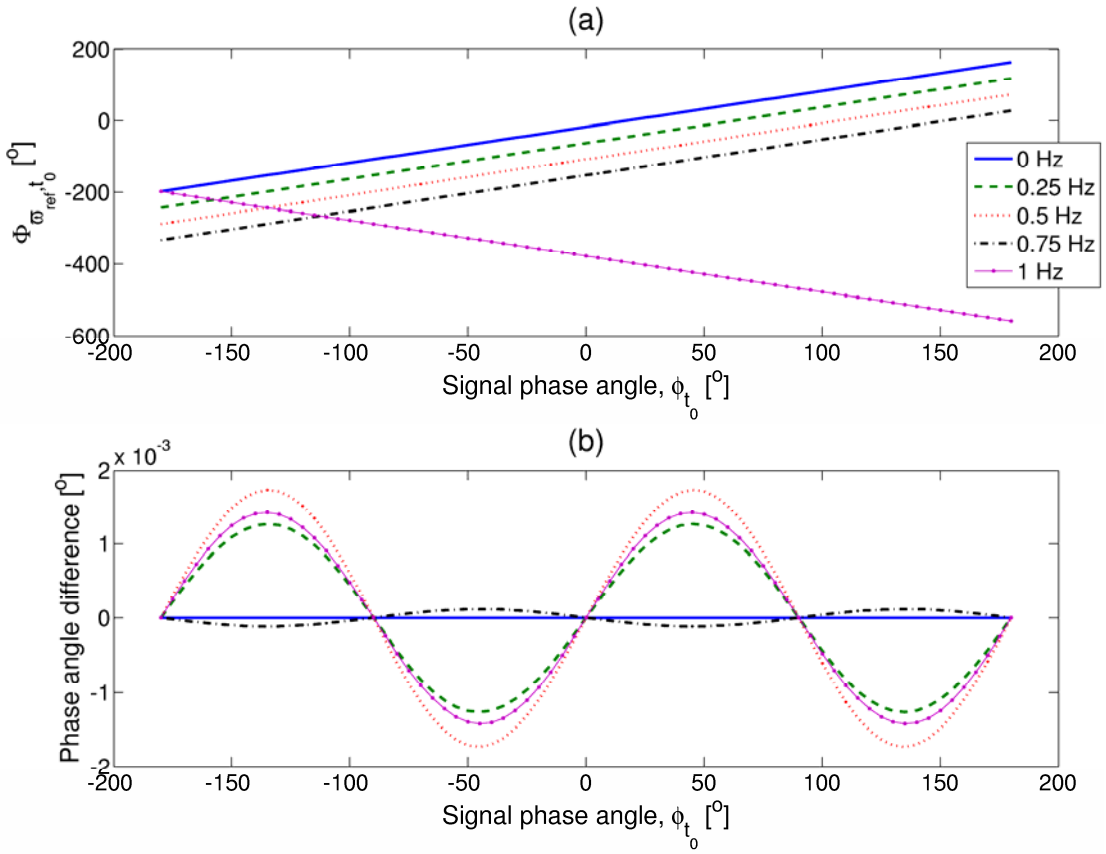

Figure 39: Phase angle detection at different frequency offsets

3.6.3 Damping

Increase in damping of a structure results in simultaneous shifts of frequency and phase. To study this phenomenon, the free vibration responses of a single degree-of-freedom mass-spring system are considered. The undamped natural frequency of the system is 35.6 Hz.

When the structural damping coefficient ζ is varied, the damped natural frequency ω_d and its corresponding phase angle ϕ_d can be calculated for free vibration responses as (Rao, 1995):

$$\omega_d = \omega_j \sqrt{1-\zeta^2}$$

Equation 39

and

$$\phi_d = \tan^{-1}\left(\frac{\zeta}{\sqrt{1-\zeta^2}}\right)$$

Equation 40

Since the introduction of structural damping also results in exponential decay of the time responses, the individual responses were normalized for comparison with results for non-normalized responses in order to study the possible effect of the decay on Φ_{ϖ_{ref},t_0}.

Figure 40 shows Φ_{ϖ_{ref},t_0} for a number of scenarios. For normalized responses with $\omega_{ref} = \omega_d$ (i.e. $\Delta\omega = 0$), Φ_{ϖ_{ref},t_0} correlates with Equation 40 and thus depicts the isolated effect of the phase angle shift. When $\varpi_{ref} = \omega_j$ (i.e. $\Delta\varpi \leq 0$), the true effects of combined phase angle and frequency shifts are observed from the normalized responses. However when the responses are not normalized, it is quite clear that the resulting exponential decays due to damping does effect Φ_{ϖ_{ref},t_0} for ϖ_{ref} at both ω_d and ω_j. In the latter case the effect is particularly pronounced. From Figure 40 it is seen that exponential decay serves to desensitize Φ_{ϖ_{ref},t_0} to frequency shift so that it mainly exhibits changes in ϕ_d.

NHFA phase angles are thus clearly affected by structural damping changes which in turn can be influenced by various operational variables such as aerodynamic damping and temperature. It will thus be necessary to keep operational variables in consideration when this condition monitoring approach is followed in an industrial environment.

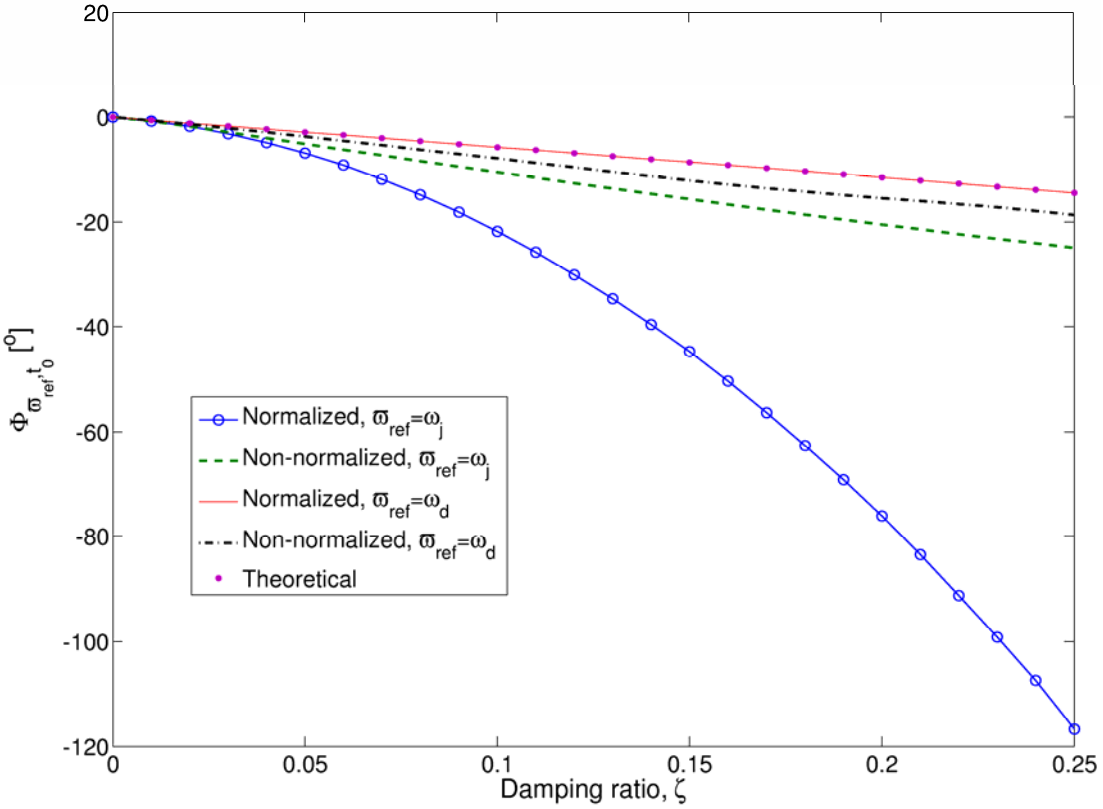

Figure 40: Effect of damping ratio on NHFA phase angle trends

3.7 Results comparison

As an initial approach, the trends of Φ are compared for the simulated ELDV results and the experimental ELDV measurements at frequencies determined from both TLDV spectral peaks and stationary modal analysis, as shown in Figure 41 in terms of Unwrapped Phase Angle (UPA) trends. Different reference frequencies were considered so as to investigate whether it is necessary to perform TLDV measurements on a rotating rotor in order to set up a condition monitoring approach, or whether the results from a simple stationary modal analysis on the rotor will suffice.

Of course, the latter approach is more desirable as it is significantly easier to perform. This does however imply the necessity of consulting FEM results when blade stiffening and/or Coriolis effects have to be taken into account, in order to adjust the stationary modal frequencies for inputs in trend calculations. Since the measurements considered in this thesis are at low rotation speeds, these rotation effects have been discarded. The various frequencies considered in this section are listed in Table 5, the numbering of which corresponds to those of the subplots in Figure 41 to Figure 44.

Table 5: Frequencies used for trend calculations

	FEM frequencies [Hz]	***Experimental frequencies [Hz]***	
	Nozzle FRF peaks	*Spectral peaks*	*Stationary modal*
(a)	124.9	131.8	126.8
(b)	624.6	620.1	628.4
(c)	818.2	844.7	820.2
(d)	1155.5	1171.9	1153.0
(e)	2273.6	2338.9	2279.3
(f)	3535.3	3588.9	3538.2
(g)	4422.2	4550.8	4447.8
(h)	6146.2	6235.4	6140.6
(i)	7495.3	7563.5	7413.1
(j)	9119.3	9238.3	9075.6

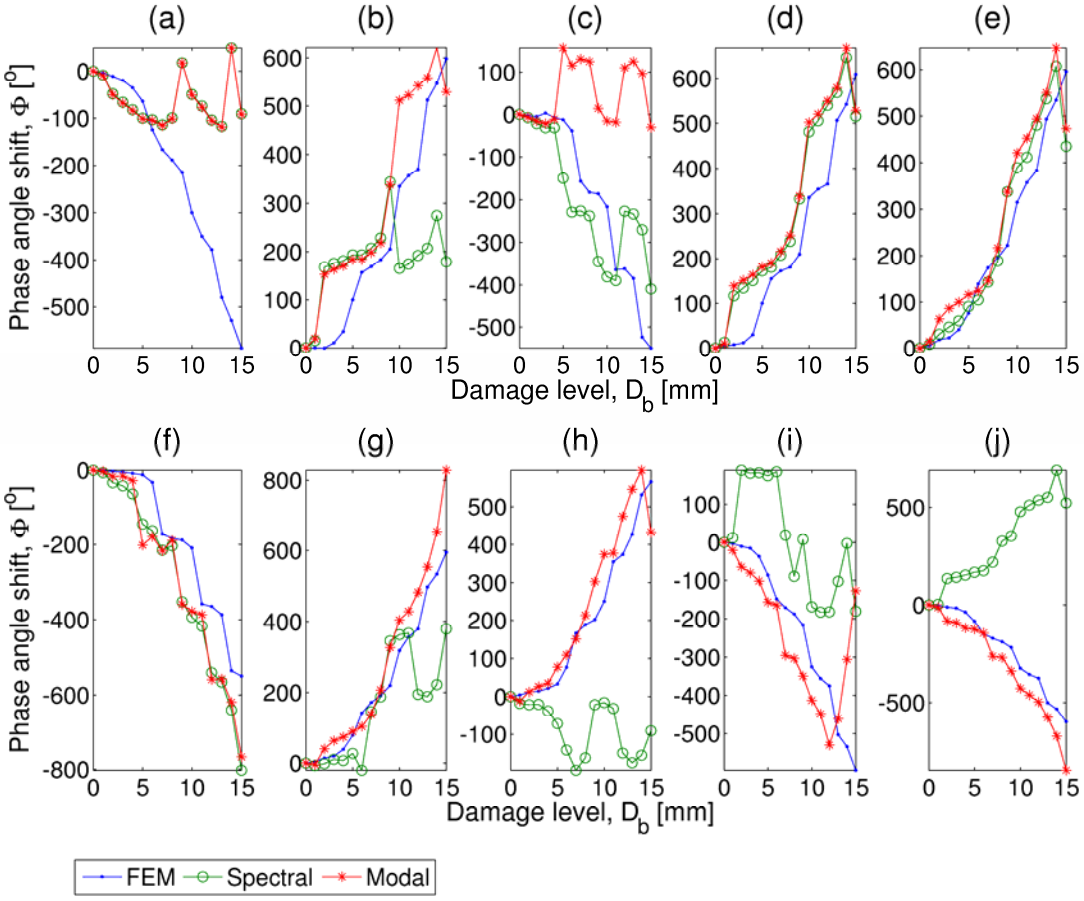

Figure 41: UPA trend comparison

Experimental UPA trend correlations with the FEM results are good at most frequencies as seen in Figure 41 for both spectral and modal reference frequencies. At some frequencies however the correlation is not satisfactory, although some correlation is present. It can be observed particularly in Figure 41(j) that the experimental UPA trend at the relevant spectral reference frequency seems to be the negative of the FEM trend. To investigate this phenomenon, UPA trends were calculated from the FEM using NHFA at the various reference frequencies over a range of ±5% of each frequency. The results are presented in Figure 42 in the form of colour maps indicating Φ corresponding to the provided colour bars. Specifically for the reference frequencies (f) to (j), a number of very distinct and abrupt UPA trend slope sign changes are visible within the specified ranges.

Upon further investigation it was discovered that these discrepancies typically occur at half-harmonics of the fundamental frequency, i.e. when $\varpi_{ref} = m\varpi_0/2$. This phenomenon is indicated on Figure 42. The same is observed for similar calculations on experimental ELDV measurements at the modal reference frequencies (Figure 43).

One approach to overcoming these trend slope sign discontinuities is to calculate the maxima of the absolute UPA trends or the Maximum Absolute Unwrapped Phase Angle Trends (MAUPATs) over the ±5% frequency ranges. In Figure 44, this approach is shown to be successful. With the exception of the first frequency, a good overall correlation is obtained at the various frequencies, showing comparable results at both spectral peak and modal reference frequencies. At the first frequency, some correlation is however still visible up to a damage level of 7 mm.

Furthermore, it is also evident that the results of stationary modal analysis are suitable for obtaining the experimental trends.

A flow diagram of the MAUPAT calculation procedure is given in Figure 45.

3.8 Experimental measurement uncertainty

Experimental measurement uncertainty is an issue that needs to be addressed. It was already discussed in Section 3.2.2 how misalignment effects could affect the TLDV measurements and how filtering was employed to negate its effects. Misalignment will manifest itself in the ELDV measurements as a DC offset proportional to the rotor speed.

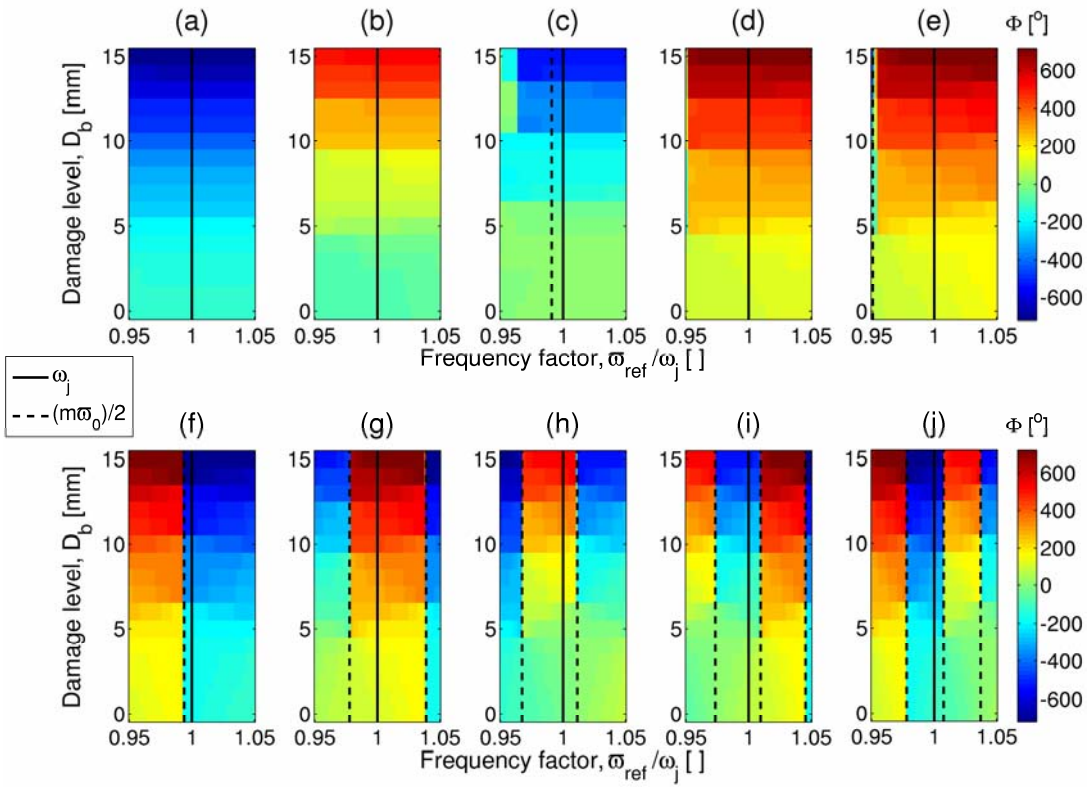

Figure 42: FEM UPA trend sensitivity analysis

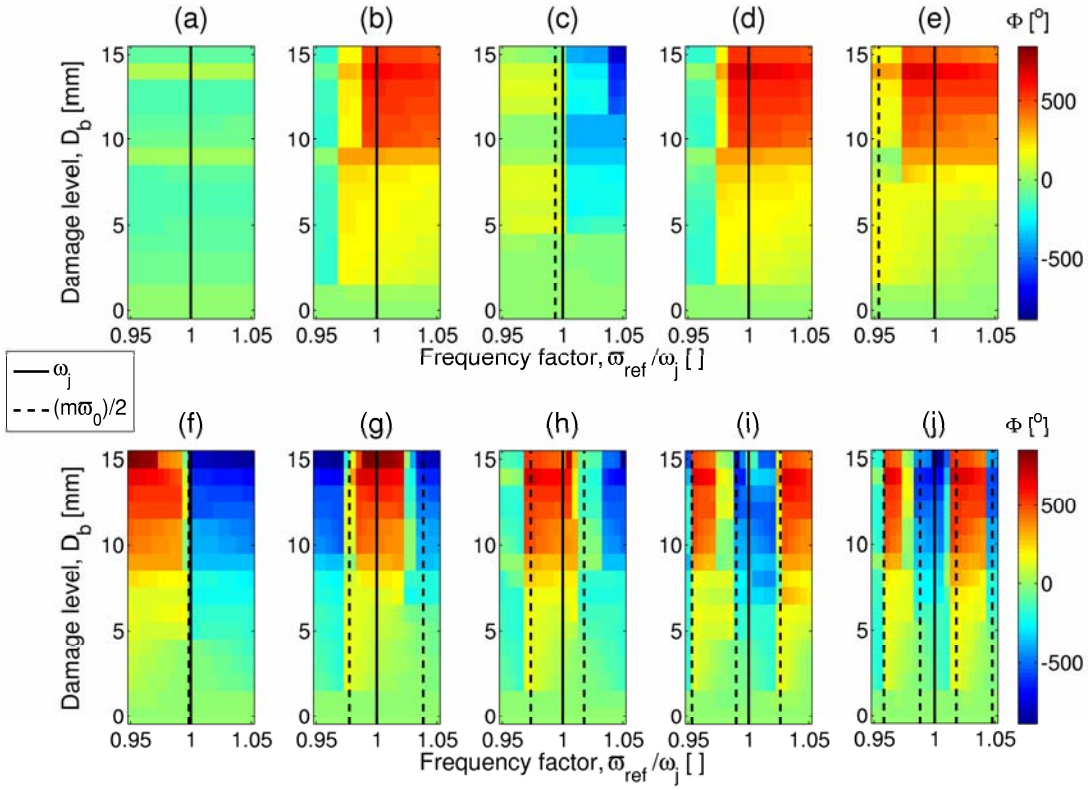

Figure 43: Experimental modal frequency UPA trend sensitivity analysis

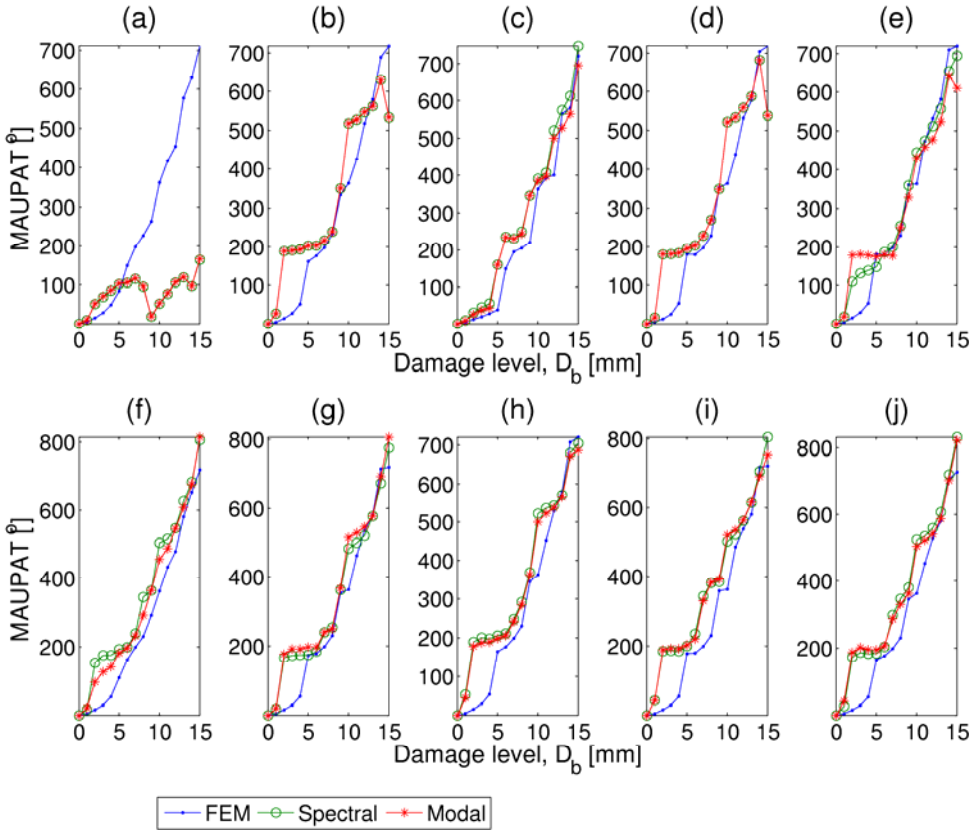

Figure 44: MAUPAT comparison

The major source of uncertainty in the ELDV measurements is speckle noise. It was assumed in this work that the speckle noise pattern remained largely constant for each damage level (Martarelli and Ewins, 2006). In an industrial environment, the speckle pattern of each blade may change over time due to deposit on the blade surface. Thus the isolated effect of speckle noise pattern change on the MAUPAT results needs to be investigated in further work.

The experimental ELDV results presented in Section 3.7 are thus influenced by misalignment effects as well as speckle noise. This may explain the trend incoherence observed between the experimental and FEM trends for the first reference frequency (Figure 44a). The greater majority of the experimental results are however validated by the FEM results.

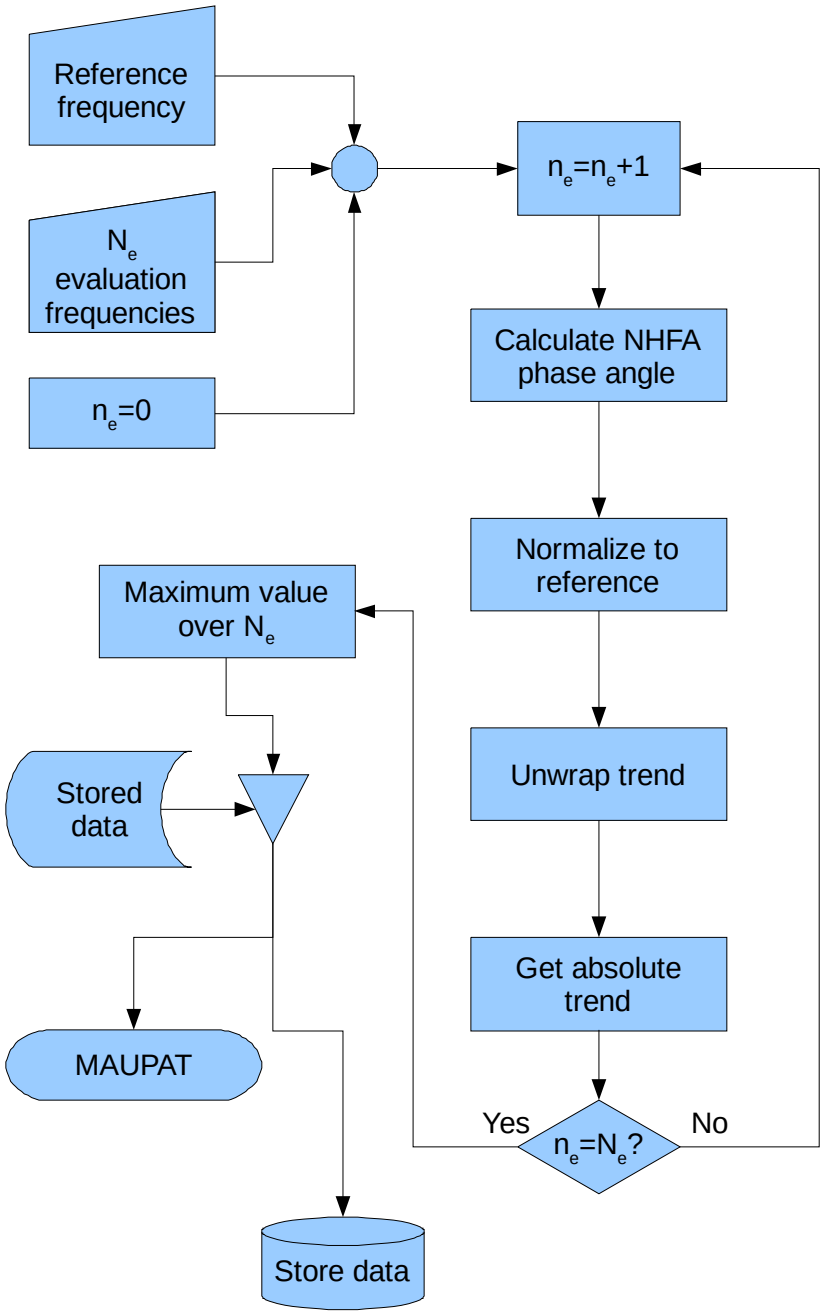

Figure 45: MAUPAT calculation flow diagram

3.9 Conclusions

This chapter serves to present new results for using ELDV on axial-flow rotor blades for the purpose of on-line condition monitoring. Some experimental results were presented for a single-blade test rotor at a rotation speed of 720 RPM. Various signal processing approaches were considered in this chapter and the NHFA technique proposed by Hirata (2005) was studied in detail.

It was shown analytically that the componential NHFA phase angle can be used to indicate signal frequency and phase angle changes when performed at reference frequencies. In a structure such as a rotor blade these changes can be brought on by damage, making NHFA phase angle trends promising as blade health deterioration indicators. With the aid of FEM predictions, this chapter shows that ELDV is a feasible measurement technique for on-line blade vibration monitoring when employing NHFA in this way.

The monitoring approach presented in this chapter should be verified at higher rotation speeds and measurements are necessary on a multi-bladed rotor to investigate whether the monitoring approach can successfully distinguish a damaged blade from amongst healthy blades.

The FEM simulation approach should also be further refined.

The work of this chapter is contained in the article titled *"Online condition monitoring of axial-flow turbomachinery blades using rotor-axial Eulerian laser Doppler vibrometry"* (Oberholster and Heyns, 2009). The results of the NHFA study (section 3.6) are summarized in the conference paper *"A study of the non-harmonic Fourier analysis technique"* (Oberholster and Heyns, 2008).